Felix Hartung,[1] *Michael Hindemith,*[2] *Matthias Wangenheim,*[2] *and Michael Kaliske*[1,3]

Frictional Abrasion of Rubber: Transition from Sliding to Rolling

REFERENCE: Hartung, F., Hindemith, M., Wangenheim, M., and Kaliske, M., **"Frictional Abrasion of Rubber: Transition from Sliding to Rolling,"** *Tire Science and Technology*, TSTCA, Vol. XX, No. X, Month 2024, pp. XX–XX.

ABSTRACT: To develop applicable friction and wear models on tire scale, reliable test data are required. Consequently, friction tests on block level are requested because the distribution of contact pressure as well as slip velocity is nearly homogeneous at the contact surface of the sliding rubber block. However, wear mechanism and energy intensity levels of sliding rubber blocks and rolling rubber wheels or tires differ significantly. Consequently, linking both sliding and rolling frictional abrasion is required; thus, a wear model for rubber material is introduced to consider both deformation slip and sliding. The model input for sliding friction and resulting wear rate is derived from linear friction test experiments using sliding rubber blocks at different loading. A unique and sophisticated re-mesh algorithm ensures proper mesh modification due to abrasion of the structure. A wear energy evolution approach is developed to consider low abrasion with small sliding distances to predict wear at rolling rubber wheels. The simulation framework of abrasion modeling is successfully validated using laboratory abrasion tests.

KEY WORDS: frictional abrasion, linear friction tester, laboratory abrasion tester, modeling wear, re-mesh algorithm, finite element analysis

Introduction

Wear as consequence of frictional abrasion arises from physical separation due to microfracture, chemical dissolution, or melting at the contact medium. In this study, the terms abrasion and wear are used synonymously, with wear classified into several types: adhesive, abrasive, corrosive, and fatigue. In the laboratory, mainly short-term wear phenomena (adhesive or abrasive wear) are investigated using, e.g., linear friction tester (LFT) [1–3] or laboratory abrasion tester (LAT) [4–8] to analyze rubber wear. In the tire industry, however, knowledge of long-term (fatigue) wear is of even greater interest. In contrast to LFT, where pure sliding between the rubber block and its abrasive substrate is observed, results of LAT100 originate from different mechanisms, such as deformation slip and short-time sliding, because on LAT100, the applied rubber wheel, which is driven by a rough spinning disc, is almost in free rolling

[1] Institute for Structural Analysis, Technische Universität Dresden, 01062 Dresden, Germany
[2] Institute of Dynamics and Vibration Research, Leibniz Universität Hannover, 30167 Hannover, Germany
[3] Corresponding author. Email: michael.kaliske@tu-dresden.de

conditions. Hence, the longitudinal slip is almost 0 and the side slip rises as the slip angle increases.

In the literature, different approaches to relate contact quantities such as contact pressure, sliding velocity, friction coefficient, and friction energy as well as frictional energy rate or power vs wear are described. Because abrasion, especially fatigue wear, acts on microscopic length scales, usually empirical models are applied to describe wear on the macroscale. Archard's wear model [9], also known as the Reye–Archard–Khrushchov wear law,

$$m_w = \frac{k}{H} F_N L, \tag{1}$$

takes normal contact forces (F_N), sliding distance (L), material hardness (H), and wear coefficient (k) into account. Moldenhauer and Kröger [1] propose a link between contact pressure (p), sliding speed (v), and friction coefficient (μ) to compute the abrasion rate, i.e.,

$$\frac{\partial m_w}{\partial x} = \mu k_w \left(\frac{p}{p_{\text{ref}}}\right)^{k_p} \left(\frac{v}{v_{\text{ref}}}\right)^{k_v}, \tag{2}$$

where kw, p_{ref}, k_p, v_{ref}, and k_v are model parameters to be identified. Kahms and Wangenheim [3] characterize the influence of the sliding velocity in a wide range and contact pressure as rational and quadratic functions, respectively, toward mass loss rate with respect to the elapsed driving distance in

$$\frac{\partial m_w}{\partial x} = \mu \left| k_{r0} \frac{k_{r1} v^2 + k_{r2} v^2}{v^2 + k_{r3} v + k_{r4}} k_{p1} \left(k_{p1} p^2 + k_{p2}\right) \right|, \tag{3}$$

with k_{r0}, k_{r1}, k_{r2}, k_{r3}, k_{r4}, k_{p0}, k_{p1}, and k_{r2} as wear model parameters. Furthermore, Grosch [4] states that abrasion (with respect to elapsed distance)

$$\frac{\partial V_w}{\partial x} = V_{w,x,\text{ref}} \left(\frac{p}{p_0}\right)^n \tag{4}$$

is generally a nonlinear function of p. However, Schallamach and Turner [10] show a correlation between friction energy and volume loss

$$V_w = \gamma \mu F_N L, \tag{5}$$

where the frictional energy is simplified as $\mu F_N L$. This formulation is the basis for many other studies. For example, in [5], the abrasion rate law

$$\dot{V}_w = k_w \dot{E}_f^{a_w} \tag{6}$$

constitutes a nonlinear relation between friction energy rate and volume loss rate that additionally takes directional effects into account. Furthermore, the abrasion rate

$$\frac{\partial \dot{V}_w}{\partial A} = k_w \left(\frac{\partial \dot{E}_f}{\partial A} \right)^{a_w} \tag{7}$$

is referred to the contact area, as proposed in [7] and [11]. In this work, Eq. (7) is applied to predict wear volume as a postprocessing procedure by using the finite element method (FEM) to compute the friction features (see "Wear Model"). Furthermore, an energy evolution law is implemented to transfer the wear model from sliding to rolling abrasion, because LFT tests at small sliding intervals show unsteady wear rate (see later). This reflects the transition from sticking to sliding in contact very well. For example in [3], the transition between deformation slip and sliding slip is modeled with the help of the brush model.

As soon as the volume to be abraded is computed, the geometry of the finite element (FE) mesh needs to be updated. In [12], the wear height results of volume loss and associated nodal area are applied along the element edges in the reference configuration (undeformed state). Alternatively, the wear direction can be defined as the inward surface normal vector, where the normal node vector is obtained by averaging the normal vectors of the attached element faces [7]. In previous work [2], a combination of [7] and [12] is implemented, i.e., the abrasion vectors at leading and trailing edges follow the corresponding element face orientations where the inner nodes are abraded normal to the contact surface. The current mesh modification approaches do not ensure that the computed wear volume (typically evaluated at FE nodes) agrees with the wear volume that is caused by moving the nodes (actual re-meshing). Hence, a new re-mesh algorithm is proposed in "Wear Model."

In accordance with [2, 3], and [13], LFT test results are used to parameterize the friction as well as the wear model in this work, whereas LAT tests are applied for model validation. In the following section, the experimental setup is described, i.e., LFT and LAT investigations using rubber block and rubber wheel samples under sliding and rolling conditions, respectively. The constitutive law used for modeling rubber is described in previous work [2]. The introduction of the friction model as well as the wear model in combination with a re-mesh algorithm that modifies the underlying FE mesh according to the computed (nodal) wear volume as output of the wear model is presented in "Friction Model" and "Wear Model," respectively. In "Model Validation," the proposed models are validated using the experimental output of "Experimental Setup." Finally, the results are concluded and an outlook for further research is presented in "Conclusions and Outlook."

Experimental Setup

The objective of this study is to apply the output of linear friction and abrasion tests by using rubber block samples to predict abrasion on LAT by using rolling rubber wheels. During linear friction tests, the distribution of contact

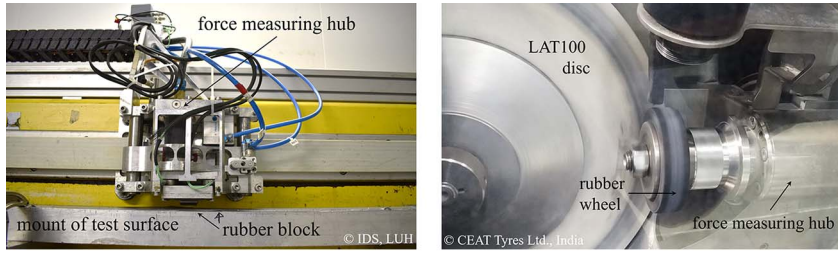

(a) Linear friction tester (HiLiTe) (b) Laboratory abrasion tester (LAT100)

FIG. 1 — *Linear friction and LAT.*

pressure as well as slip velocity are nearly homogeneous at the contact to the substrate. The homogeneity of the contact quantities is required to apply the friction and wear models introduced in "Friction Model" and "Wear Model." In Fig. 1, the test devices for LFT (HiLiTe) and LAT (LAT100, VMI) are displayed.

The HiLiTe test rig shown in Fig. 1a allows friction coefficient investigations of tire tread blocks on different track surfaces and different ambient conditions. In [2], a detailed description of the test rig is given. Preconditioning the block samples by several sliding passes (see [2]) leads to initial wear of the sample finally resulting in a homogeneous pressure and temperature distribution throughout the contact area.

Initially, friction and abrasion tests on LFT are performed on sandpaper grit 60 with the assumption to produce comparable output as the LAT device where a disc grit 60 is applied. Although the friction performance is in a similar range, the mass loss is overestimated by a factor of approximately 2 to 4, which is observed using an LAT disc as substrate at LFT tests (see later). In Fig. 2, the different abrasion residues on sandpaper and on LAT disc are demonstrated.

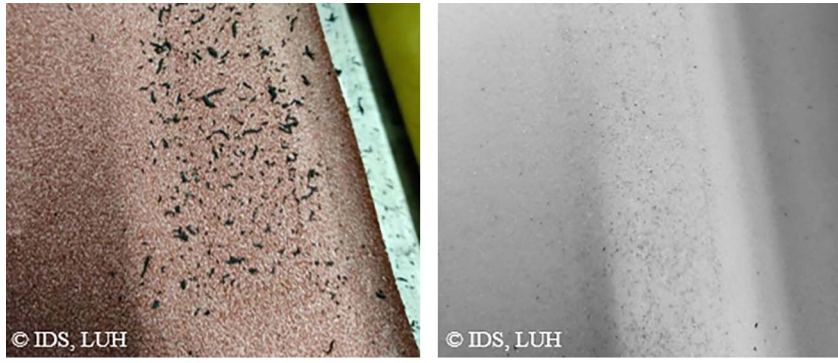

(a) Sandpaper grit 60 (b) LAT disc grit 60

FIG. 2 — *Abrasion residue on sandpaper grit 60 and on LAT disc grit 60.*

TABLE 1 — *LFT test conditions on sandpaper grit 60 and LAT disc grit 60.*

Parameter	Sandpaper	LAT disc
Load p_N, N/mm^2	$\{0.4, 0.8, 1.2, 1.4, 1.6\}$	$\{0.4, 0.8\}$
Speed v_x, mm/s	$\{10, 50, 100, 1000, 3000\}$	$\{1, 10, 110, 320, 1090, 1910\}$
Driving distance, mm	500–600	270
Powder	No	Yes

Hence, the abrasion tests are repeated using the same disc that is applied for the LAT tests. In addition, the same powder mixture, which reduces the influence of sticking rubber particles during LAT experiments, is put on the LAT disc during LFT abrasion tests. The underlying powder is a mixture of aluminum oxide (Al_2O_3) and magnesium oxide (MgO), with a mass ratio of 2.15:1 (Al_2O_3:MgO). Before each test run, a sufficient quantity of powder is applied to the road surface by using an automatic powder dosing device. The amount of powder per test run is derived from official LAT protocols by the LAT100 manufacturer. Table 1 presents the conditions for LFT friction and abrasion tests.

The driving speeds are derived from LAT pure side slip testing conditions $v_{x,\mathrm{LFT}} = \sin(\alpha)\, v_{x,\mathrm{LAT}}$ with the slip angle α. The ambient and the surface temperatures are adapted iteratively during the LFT abrasion tests to obtain comparable contact temperatures as recorded in the LAT experiments for similar sliding velocities. The measured (sliding) friction coefficient and mass loss rate are shown in Fig. 3.

Note that the friction coefficient decreases to larger load (compare blue, red, yellow, and purple solid lines in Fig. 3), whereas the mass loss rate increases (compare blue and red dashed lines in Fig. 3). The different output of the applied substrates (sandpaper vs LAT disc) with respect to the measured friction coefficient as well as mass loss rate are shown in Fig. 4, where the

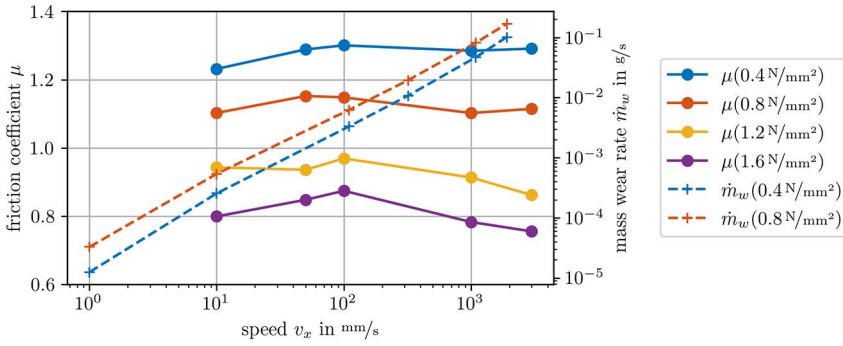

FIG. 3 — *Measured friction coefficient and mass wear rate during LFT abrasion tests.*

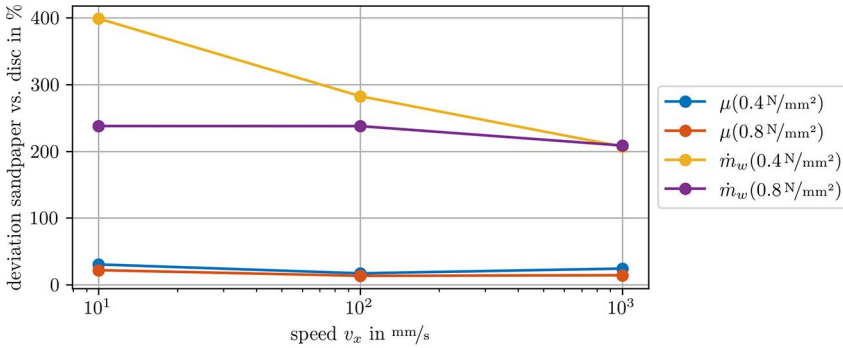

FIG. 4 — *Deviation of recorded friction and wear during LFT experiment using sandpaper grit 60 and LAT disc grit 60.*

speed values 10, 110, and 1090 mm/s of the abrasion tests are used for comparison.

The LAT100 abrasion tester consists of a driven counter-surface disc on which a solid rubber test wheel is pressed under a normal load at a slip angle for a predefined driving distance [8]. The rotational velocity of the rubber wheel is induced by the disc traveling speed. The machine records the counter-centrifugal or radial force, the side force, and the tangential friction force. As for the LFT, the mass loss is obtained by weighing the rubber sample after each test. To reproduce the LFT and LAT results with the same wear model, the test conditions have to be as similar as possible. Table 2 outlines the comparison of different boundary conditions using LFT and LAT.

The remaining differences in the abrasion tests using LFT and LAT are the applied testing device, driving maneuver, and the cleaning procedure of the LAT disc. The linear friction tests on HiLiTe are performed by the Institute of Dynamics and Vibration Research at Leibniz Universität Hannover, whereas CEAT Tyres Ltd. (Mumbai, India) conducted the LAT100 experiments. Table 3 lists all test conditions of the LAT protocol.

The speed v_x in Table 3 refers to the speed of the LAT disc at wheel position, and the slip angle coincides with the rotation around the vertical axis of the rubber wheel (see later). For each test condition, two test runs are performed

TABLE 2 — *Comparison of boundary conditions by using linear friction and LAT.*

Equal condition	Unequal condition
Rubber compound	Testing device
Load range and ambient temperature	Driving maneuver (sliding vs rolling)
Substrate (LAT disc incl. powder)	Substrate cleaning procedure
Sample dimensions	

TABLE 3 — *LAT testing protocol with* $F_z = 75\,N$.

No. run	Speed v_x, km/h	slip angle α, °	Driving distance x, m
1, 2	25	16	250
3, 4	12	16	140
5, 6	2.5	13	200
7, 8	25	9	600
9, 10	12	9	600
11, 12	2.5	9	600
13, 14	25	5.5	2500
15, 16	12	5.5	1500
17, 18	2.5	5.5	1400

to achieve uniform wear on both rubber wheel edges: a first test run without rotation and then a second test run with 180° rotation around vertical wheel axis. The recorded side force as well as the mass loss rate shown in Fig. 5 provide the base for the validation of the friction and wear models described in "Friction Model" and "Wear Model," respectively.

However, in a first validation step, LFT tests using cut rubber wheel segments are performed. To investigate similar conditions as on LAT, the wheel segment slides only few millimeters over the underlying LAT disc to mimic the stick-slip transition in contact due to the global deformation of the rotating rubber wheel during LAT experiments. Figure 6 illustrates the rubber wheel segments as well as the test setup.

For the evaluation of abrasion, the mass loss is measured over a constant sliding distance. The mass loss of the sample is recorded using a precision balance (Kern) that has a resolution of 0.1 mg [14]. For these tests, sliding distances of 4, 8, 12, 24, and 48 mm and a cumulative sliding distance of 144 mm

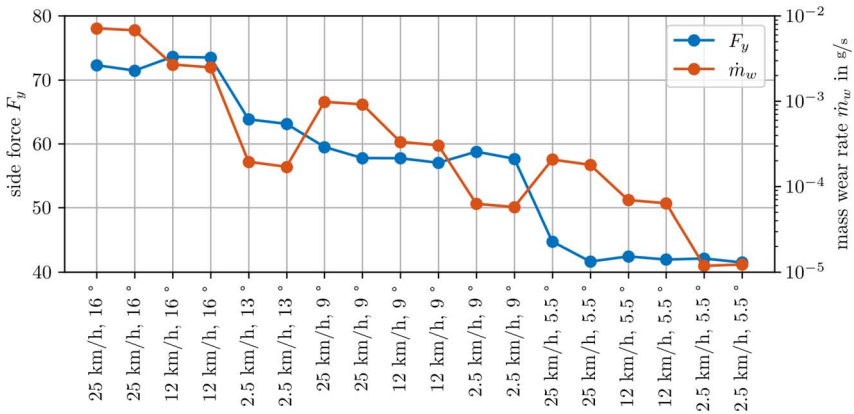

FIG. 5 — *Measured side force and mass loss rate during LAT protocol.*

FIG. 6 — *Grosch wheel segment at height of 40 mm.*

are used. The weight of the samples is measured after each 48-mm sliding distance. The multiple of the lowest sliding distance of 4 mm is used for a comparison of the influence of sticking and sliding transitions on the abrasion of the samples. Two rubber wheel segments are glued together to guarantee a stable driving phase at higher loads because the contact area is quite small. Hence, the weighted mass loss difference is divided by 2 for comparison with the output of the simulation framework introduced in "Wear Model." Table 4 shows the conditions of the LFT tests using rubber wheel segments. Note that the wheel height in Table 4 refers to the height of the rubber wheel segment (see Fig. 6, right). The short-distance sliding test results are presented in "Model Validation."

Friction Model

Friction is defined as force resisting the relative motion of solid surfaces, fluid layers, and material elements sliding against each other. It consists of different contributions such as hysteretic, adhesive, or viscous friction. In this study, a macroscopic friction formulation, which is intended to predict hysteretic and adhesive features, describes the transition of tangential forces in contact. The tangential traction vector

$$\boldsymbol{t}_T = \mu p_N \varphi_i \frac{\boldsymbol{g}_T}{\|\boldsymbol{g}_T\|} \tag{8}$$

depends on the friction coefficient (μ), the normal pressure (p_N), the regularization function (φ_i), and the relative tangential slip vector ($\boldsymbol{g}_T$) that consists of two components (perpendicular to each other). The bilinear regularization function

TABLE 4 — *LFT test conditions (short distance).*

Description	Wheel height, mm	Speed v_x, mm/s	Vertical force F_z, N
Reference	40	5	75
Height variation	25	5	75
Speed variation	40	10	75
Load variation	40	5	150

$$\varphi_1 = \begin{cases} \dfrac{\| \boldsymbol{g}_T \|}{g_{\text{crit}}} & \text{if } \| \boldsymbol{g}_T \| < g_{\text{crit}} \\ 1 & \text{otherwise} \end{cases} \tag{9}$$

provides numerical stability during sliding. The operator $\| \square \|$ represents the norm of the related tensor. For tensors of first order (vectors), the norm coincides with the vector length. This projection enables the friction model to compute the frictional response independently of the sliding direction, i.e., combined slip states such as simultaneous braking and corning are considered. Alternatively, nonlinear regularization functions, e.g., hyperbolic tangent adjustment, can be applied [15]. If the critical slip (g_{crit}) approaches 0 and μ is constant, Eq. (8) represents the Coloumb friction law. In many applications, it is required to use nonconstant friction coefficients. The Huemer friction law

$$\mu = \frac{\alpha p_N^{n-1} + \beta}{a + \frac{b}{|v_T|^{1/m}} + \frac{c}{|v_T|^{2/m}}} = c_p(p_N)\, c_v(\| \boldsymbol{v}_T \|), \tag{10}$$

which is applied in this study, defines the friction coefficient as a function of the p_N and the tangential slip velocity vector ($\boldsymbol{v}_T$). In Eq. (10), variables a, b, c, n, m, α, and β are friction model parameters to be identified (see [16]). With the help of an optimization tool based on an evolution algorithm described in [17], the function in Eq. (10) is fitted to the measured friction coefficient values (see Fig. 3) as shown in Fig. 7.

Because the investigated range of load and sliding velocity is limited during experiments, the Huemer friction function is expanded in Fig. 7 (see $\mu_{\text{fit,out}}$) to ensure the applicability of Eq. (10). The normal pressure and the sliding velocity, where $\| \boldsymbol{v}_T \|$ coincides with v_x from Fig. 7, are input for the introduced friction law in Eq. (10) to compute the friction coefficient at each contact point. Table 5 lists the identified friction parameters.

The energy generated by friction at each contact point (in case of sliding) is generally calculated by

$$E_f = F_T \| \boldsymbol{g}_T \| = \| \boldsymbol{t}_T \| A \| \boldsymbol{g}_T \|, \tag{11}$$

where A represents the contact point related contact area. Consequently, the frictional energy rate or friction power

$$\dot{E}_f = \| \boldsymbol{t}_T \| A \frac{\| \Delta \boldsymbol{g}_T \|}{\Delta t} = \| \boldsymbol{t}_T \| A \| \boldsymbol{v}_T \|, \tag{12}$$

with Δg_T as incremental slip vector, can be expressed by the slip velocity vector (v_T). By removing the related contact area in Eq. (12), the friction power is transferred to the friction power intensity (friction energy rate per area of contact).

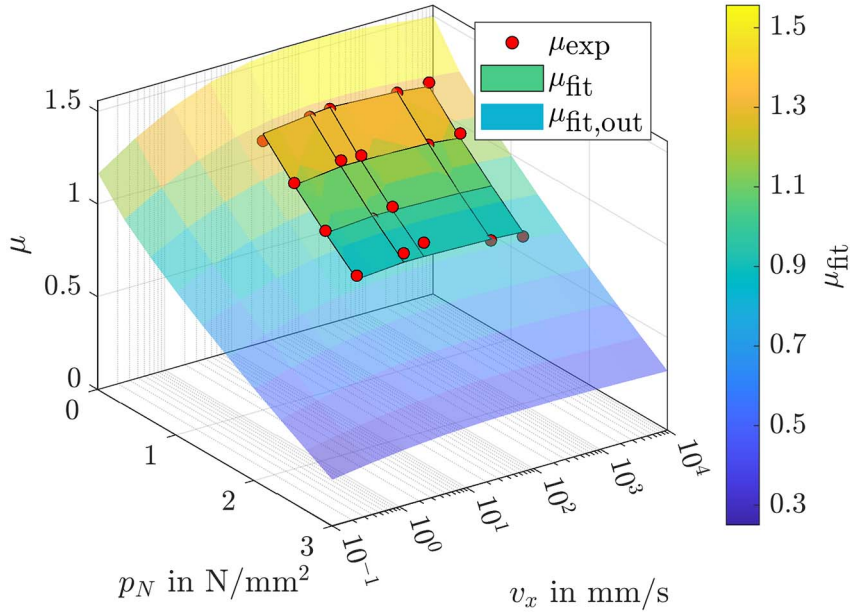

FIG. 7 — *Identification of Huemer friction model parameters by fitting Eq. (10) to LFT measurements.*

Wear Model

Wear as consequence of friction (with relative motion in the contact) between contact partners is categorized into several types: adhesive, abrasive, corrosive, and fatigue. In this work, the focus is placed on long-term or fatigue wear (no sudden separation of material). Following the findings of Archard [9] and Schallamach and Turner [10], wear directly correlates to frictional energy or frictional power. A nonlinear relationship between volume wear rate intensity

$$\frac{\partial \dot{V}_w}{\partial A} = k_w \left(\frac{\partial \dot{E}_f}{\partial A} \right)^{a_w} \tag{13}$$

and frictional power intensity is chosen. In Eq. (13), k_w and a_w are wear model parameters. Because different rubber geometries are investigated in this study (block and wheel samples), the physical quantities relate to the corresponding

TABLE 5 — *Identified Huemer friction parameters.*

a	b	C	n	m	α	β
5.109363	−4.330187	3.411753	1.758465	10.64962	−2.016165	5.882340

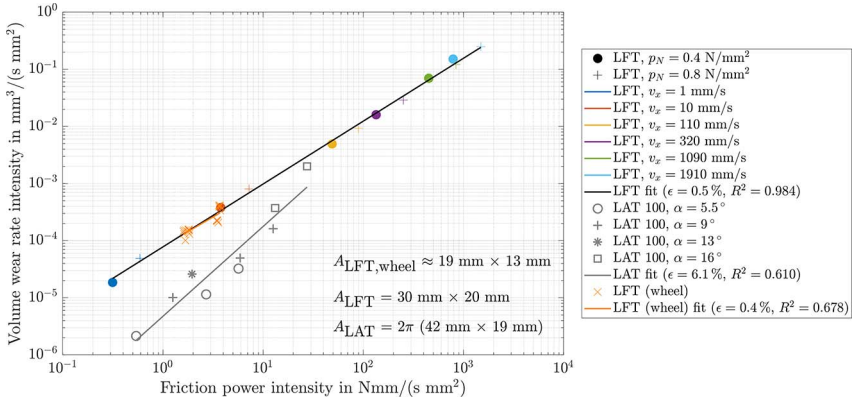

FIG. 8 — *Identification of wear model parameters.*

contact area (wear rate and friction power transferred to wear rate intensity and friction power intensity).

To identify the wear model parameters k_w and a_w, LFT tests using block samples are used. The frictional energy rate for LFT sliding blocks is estimated by

$$\dot{E}_{f,\mathrm{LFT}} \approx p_N\, \mu\, A_{\mathrm{LFT}}\, v_x\,, \tag{14}$$

where p_N and v_x refer to the applied normal pressure and sliding velocity, respectively. It is assumed that the associated contact area $A_{\mathrm{LFT}} = 30\,\mathrm{mm} \times 20\,\mathrm{mm}$ corresponds to the length and width of the rubber block sample. Symbol μ in Eq. (14) represents the friction coefficient recorded during the related LFT test. Because Eq. (13) is linear in double logarithmic scale, the least mean square method is applied to fit Eq. (13) to wear test results introduced in "Experimental Setup." The result is presented in Fig. 8, where the solid black line shows the final wear model function with $k_w = 7.783 \times 10^{-5}\,\mathrm{mm^2/N}$ and $a_w = 1.101$ (see also Table 6). The unit of the term in brackets in Eq. (13) should not be affected by wear parameter a_w to ensure unit consistency.

The resulting coefficient of determination

$$R^2 = 1 - \frac{\sum_{i=1}^{m} \left(\dot{V}_{w,\mathrm{exp},i} - \dot{V}_{w,i} \right)^2}{\sum_{i=1}^{m} \left(\dot{V}_{w,\mathrm{exp},i} - \overline{\dot{V}}_{w,\mathrm{exp}} \right)^2}\,, \tag{15}$$

where $m = 12$ corresponds to the number of different wear test conditions and $\overline{\dot{V}}_{w,\mathrm{exp}}$ stands for the averaged volume wear rate of the LFT experiments, is close to 1, i.e., the wear model can predict the experiments to the full extent in

TABLE 6 — *Identified wear model parameters.*

k_w	a_w	$E_{w,0}$	p_w
$7.783 \times 10^{-5}\,\mathrm{mm^2/N}$	1.1017	2.879 N mm	0.03

the investigated velocity range. Note that the link to the contact area is removed in Eq. (15) because the total contact area is identical for each test. The wear volume rate of the rubber block samples is derived by using a density of $1.12 \times 10^{-3}\,\mathrm{g/mm^3}$ [2]. In addition, the deviation of LAT test results described in "Experimental Setup" with respect to wear are visualized in Fig. 8. The orange markers and the short orange line refer to short distance tests performed on LFT by using rubber wheel segments (see "Experimental Setup" and "Model Validation"), which fit perfectly to the LFT tests results by using block samples.

By LFT tests using small driving distances, we observed that the wear energy rate evolves until a certain plateau value is reached (see later). This reflects the transition from sticking to full sliding via states of local microslip in the contact. Globally, on wheel scale, this corresponds to the transition from deformation slip to sliding slip. Therefore, an energy-based evolution law is linked to the wear model. In Eq. (13), the frictional energy rate is replaced by the wear energy rate

$$\dot{E}_w = f_w \dot{E}_f \tag{16}$$

with

$$f_w = \tanh\left[\frac{E_f\, 0.5 \log\left(\frac{2-p_w}{p_w}\right)}{E_{w,0}}\right], \tag{17}$$

which increases by the incorporated friction energy. If $f_w = 0$, no friction energy rate is transmitted as wear energy rate. As soon as $f_w = 1$, the friction energy rate is equal to the wear energy rate. Parameters $E_{w,0}$ and p_w in Eq. (17) need to be quantified by wear experiments. Equation (17) is comparable to the hyperbolic tangent regularization described by Wriggers [15]. In Fig. 9, an evaluation of the evolution function f_w shows the transition from deformation slip ($\dot{E}_w = 0$) to full sliding slip ($\dot{E}_w = \dot{E}_f$). The intermediate region is associated to local microslip (local slip). Table 6 lists all identified wear model parameters.

Because Eq. (13) is applied at every contact node, the corresponding volume loss rate has to be transferred to a node displacement due to wear. Typically, the wear height or the length of wear displacement vector results from volume loss and associated nodal area [2, 7, 12]. However, it is not guaranteed

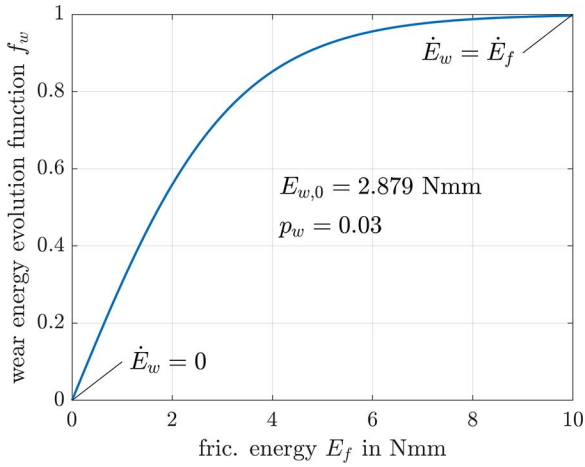

FIG. 9 — *Wear energy rate evolution function.*

that the computed wear volume coincides with the wear volume that is caused by moving the nodes in contact by the corresponding wear height (referred to as "re-meshed wear" hereafter). Hence, in this work, a re-mesh algorithm is introduced to minimize the difference between computed and re-meshed wear volume. Consequently, the update of the mesh geometry due to wear is directly connected to the underlying wear model [see Eqs. (13) and (16)] and thus more reliable The basic idea is to set the remaining volume at the integration points (due to re-meshed wear) equal to the nodal volumes projected to the corresponding integration points (due to computed wear), i.e.,

$$\det\left[\underline{\boldsymbol{F}}_i(\boldsymbol{w})\right] \mathrm{d}V_i \;=\; \mathrm{d}v_I \, N_I(\boldsymbol{\xi}_i)\,, \tag{18}$$

where $\underline{\boldsymbol{F}}_i$ is the deformation gradient at integration point i, $\boldsymbol{w}$ represents the vector of wear displacement factors (explained in the following), $\mathrm{d}V_i$ coincides with the unworn integration point volume in the current configuration, $\mathrm{d}v_I$ is the nodal volume after wear at node I (also in the current configuration), and N_I stands for the associated element shape function at the natural coordinates $\boldsymbol{\xi}_i$ of integration point i. Figure 10 visualizes some of the quantities introduced on an FE mesh of a wheel-shaped sliding body in the current configuration.

Using Eq. (18), a system of equations for all integration points of one contact element is set up that is solved iteratively by the Newton–Raphson method

$$\frac{\partial \boldsymbol{f}(\boldsymbol{w}^{[n]})}{\partial \boldsymbol{w}^{[n]}} \cdot \Delta \boldsymbol{w} + \boldsymbol{f}(\boldsymbol{w}^{[n]}) \;=\; 0\,, \tag{19}$$

with

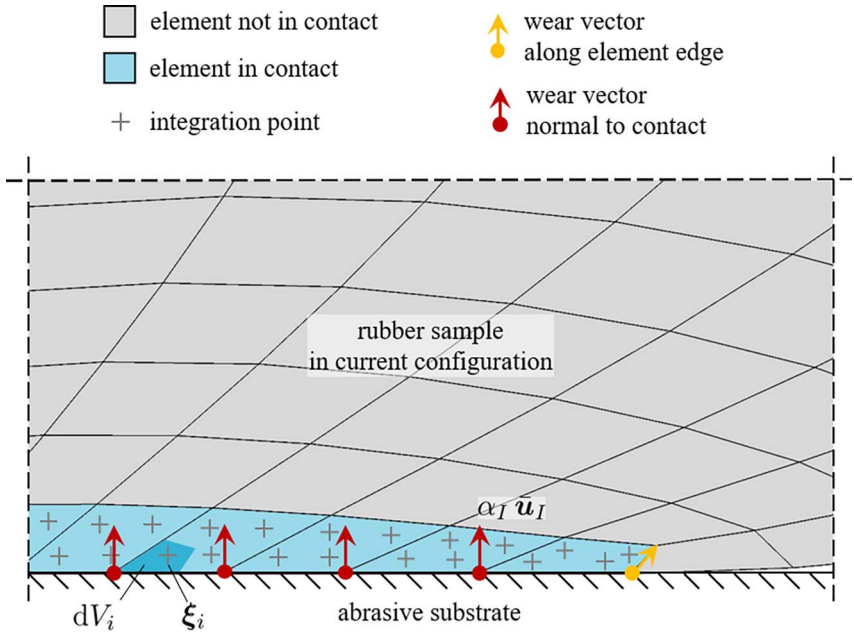

FIG. 10 — *Re-meshing of FE rubber sample.*

$$f_i(\boldsymbol{w}^{[n]}) = \det\left[\underline{\boldsymbol{F}}_i(\boldsymbol{w}^{[n]})\right] \mathrm{d}V_i - \mathrm{d}v_I \, N_I(\boldsymbol{\xi}_i) \tag{20}$$

as residual equation for each integration point i at iteration step n. In Eqs. (19) and (20), vector $\boldsymbol{w}$ represents the wear displacement factors of all nodes of the contact element, which are equal to the length of the related wear displacement vectors. The incremental change of the wear displacement factors from one iteration step to another is expressed by

$$\Delta \boldsymbol{w} = \boldsymbol{w}^{[n+1]} - \boldsymbol{w}^{[n]} \, . \tag{21}$$

The derivative in Eq. (19) can be rewritten as

$$\begin{aligned} \frac{\partial f_i(\boldsymbol{w}^{[n]})}{\partial \boldsymbol{w}^{[n]}} &= \frac{\partial \det\left[\underline{\boldsymbol{F}}_i(\boldsymbol{w}^{[n]})\right]}{\partial \boldsymbol{w}^{[n]}} \mathrm{d}V_i \\ &= \left[\frac{\partial \det \underline{\boldsymbol{F}}_i}{\partial \underline{\boldsymbol{F}}_i} : \frac{\partial \underline{\boldsymbol{F}}_i(\boldsymbol{w}^{[n]})}{\partial \boldsymbol{w}^{[n]}}\right] \mathrm{d}V_i \end{aligned} \, , \tag{22}$$

for each integration point i using the identity

$$\frac{\partial \det \underline{\boldsymbol{F}}_i}{\partial \underline{\boldsymbol{F}}_i} = \det(\underline{\boldsymbol{F}}_i) \, \underline{\boldsymbol{F}}_i^{-T} \tag{23}$$

and the derivative

$$\frac{\partial \underline{\boldsymbol{F}}_i(\boldsymbol{w}^{[n]})}{\partial \boldsymbol{w}^{[n]}} = \frac{\partial\left[\partial \boldsymbol{u}_i(\boldsymbol{w}^{[n]})/\partial \boldsymbol{w}^{[n]}\right]}{\partial \xi_i} \cdot \underline{\boldsymbol{J}}_i{}^{-1}, \tag{24}$$

with

$$\underline{\boldsymbol{F}} = \text{Gradu} + \underline{\boldsymbol{I}} = \frac{\partial \boldsymbol{u}}{\partial \boldsymbol{X}} + \underline{\boldsymbol{I}} \tag{25}$$

and

$$\frac{\partial \boldsymbol{u}}{\partial \boldsymbol{X}} = \frac{\partial \boldsymbol{u}}{\partial \xi} \cdot \frac{\partial \xi}{\partial \boldsymbol{X}} = \frac{\partial \boldsymbol{u}}{\partial \xi} \cdot \underline{\boldsymbol{J}}^{-1}. \tag{26}$$

The second order tensor $\underline{\boldsymbol{J}}$ is also known as Jacobi matrix. In Eq. (24), the displacement vector

$$\underline{\boldsymbol{u}}_i = \sum_{I=1}^{n_e} N_I(\xi_{\boldsymbol{i}})\, \mathrm{u}_I\left(w_I{}^{[n]}\right), \tag{27}$$

with n_e as number of element nodes, stands for the displacement vector due to wear associated with integration point i. The derivative of the node displacement vector $\boldsymbol{u}_I$ with respect to the wear displacement factor $w_I{}^{[n]}$ is expressed by

$$\frac{\partial \boldsymbol{u}_I\left(w_I{}^{[n]}\right)}{\partial w_I{}^{[n]}} = \begin{cases} \overline{\boldsymbol{u}}_I & \text{if } w_I \neq 0 \\ 0 & \text{otherwise} \end{cases}, \tag{28}$$

where $\overline{\boldsymbol{u}}_I$ represents the unit-length wear node direction vector at node I. The wear node direction vector points either along an element edge or toward the normal direction of the corresponding contact node (derived by averaging over attached element faces), which is shown in Fig. 10. As soon as Eq. (19) is assembled for all contact elements, the system of equations is overdetermined because the number of integration points is larger than the number of independent wear displacement factors at all contact nodes and thus the wear node displacement factors $\boldsymbol{w}$ must be updated iteratively. Wear node displacement factors at contact element nodes, that are not in contact, are set to 0. As soon as the residuum

$$\| \boldsymbol{r}(\boldsymbol{w}^{[n]}) \| < \epsilon \text{ with } r_i(\boldsymbol{w}^{[n]}) = -\frac{f_i(\boldsymbol{w}^{[n]})}{\det\left[\underline{\boldsymbol{F}}_i(\boldsymbol{w}^{[n]})\right] \mathrm{d}V_i} \tag{29}$$

is lower than a predefined limit ϵ (e.g., 10^{-3}) or a maximum number of iterations is performed (e.g., 10), the Newton–Raphson iteration terminates. The residuum $\boldsymbol{r}$ can be interpreted as the length of the relative volume differences of the integration points in contact elements. During re-meshing, Eqs.

(18)–(29) are applied for each time step t_j. The final wear node displacement vector $\boldsymbol{U}_I$ is applied to each node I in the reference configuration by

$$\boldsymbol{U}_I = \sum_{j=1}^{n_t} \underline{\boldsymbol{F}}_I^{-1}(t_j) \cdot \boldsymbol{u}_I(t_j), \tag{30}$$

with n_t as number of time steps and $\underline{\boldsymbol{F}}_I^{-1}$ as inverse of the deformation gradient projected to node I. In "Model Validation," the performance of the developed re-mesh algorithm is presented in detail. The wear model as well as the re-mesh algorithm are implemented into a (postprocessing) simulation framework, which is outlined in Fig. 11.

After setting up simulation parameters, e.g., boundary conditions (load, driving speed, incremental driving distance [Δd]) and wear model parameters, the simulation chain starts as a loop over all defined driving steps. One step could be free-rolling followed by braking and so forth. As soon as the FEM simulation is completed successfully, the model data (mainly mesh geometry) are imported into the postprocessing tool. If the FEM simulation bases on an arbitrary Lagrangan Eulerian (ALE) approach (see [18, 19]) to model steady-state conditions, a timeline is introduced by computing time increments

$$\Delta t_j = \varphi_j / \Omega \tag{31}$$

for each streamline, where φ_j and Ω represent the angle of sector j and the rotational velocity, respectively. In the next step, the time-dependent contact output such as contact shear stresses and tangential slip velocity is read from the simulation output to calculate the frictional energy rate intensity in Eq. (12). Finally, the re-mesh algorithm is applied to update the node coordinates of the elements in contact using a predefined Δd. If ALE simulations are performed, wear is applied on a periodic sector that is thereupon revolved to a fully three-dimensional model (e.g., wheel or tire model). The FEM simulation is restarted using the same boundary conditions and the updated mesh geometry until the desired driving distance ($d_{\text{step},i}$) of step i is reached. Subsequently, the next driving step $i + 1$ can be performed where different boundary conditions may be applied but the mesh is taken over from the final re-meshing run of the current driving step i. The step-related elapsed driving distance d_i is set to 0 again. Note, that the value of the Δd may influence the re-meshing result. For severe driving conditions (e.g., braking), it is recommended to perform a convergence study with respect to Δd and the corresponding change in mesh geometry.

Model Validation

Because the sliding distance on LAT is rather small (maximum of a few millimeters), the implemented simulation framework shown in Fig. 11 is

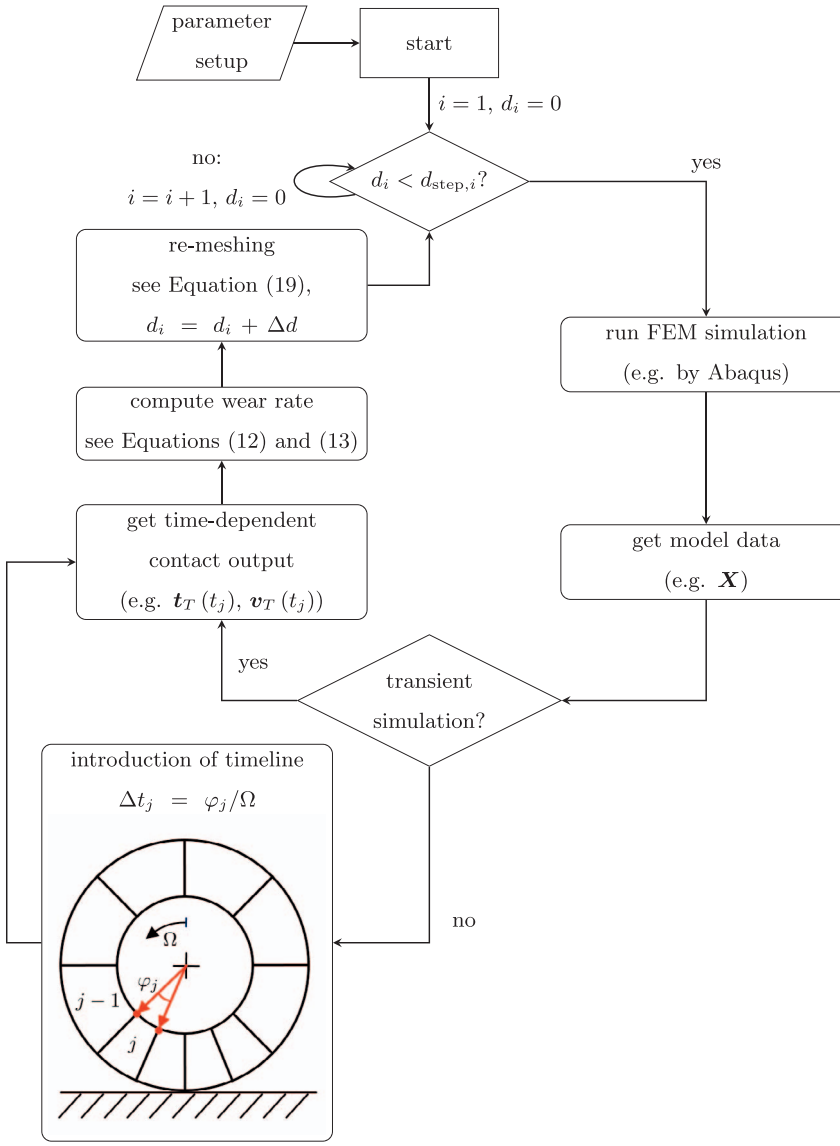

FIG. 11 — *Simulation framework of abrasion modeling.*

validated initially by short-distance sliding tests by using linear friction tests with Grosch wheel segments on an LAT disc (see Fig. 6). The applied FE model is displayed in Fig. 12, where the top surface is fixed to the mounting plate (neither translation nor rotation allowed).

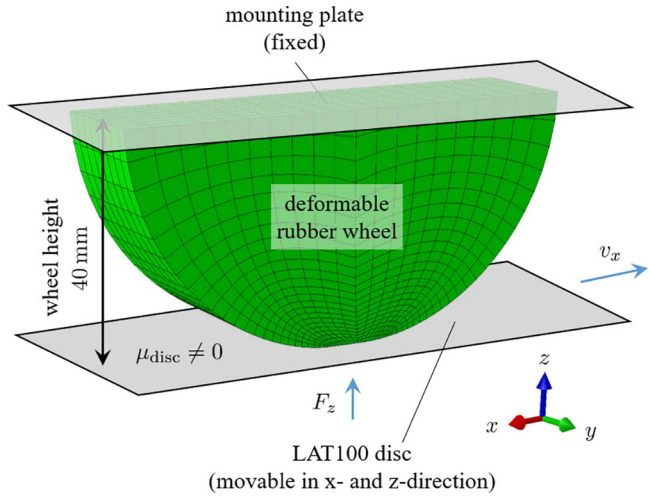

FIG. 12 — *FE model of sliding Grosch wheel segment.*

The substrate surface is first pressed toward the rubber wheel segment followed by sliding against the positive x-direction. The Huemer friction law described in "Friction Model" is used as μ_{disc}. The re-mesh algorithm is applied onto the entire contact region, because the substrate surface slides (time dependent) against the rubber wheel (no periodic sector model because no ALE approach). Different rubber wheel heights, driving speeds, and vertical loads are investigated with respect to volume loss rate (see Table 4). The density of the rubber is considered as $1.12 \times 10^{-3}\,\text{g/mm}^3$ [2]. The Δd for each driving step coincides with the related driving distances of 4, 8, 12, 24, and 48 mm because there is only a slight change in the mesh geometry due to abrasion. Figure 13 compares the simulation results with the LFT wear measurements.

The order in wear rate magnitudes fits to the experiments, whereas the simulation reproduces the experimental results perfectly at small load and driving speed. Note that the experiments as well as the simulations consist of a wear rate ramping until a constant wear rate is reached. The transition from ramping to the plateau of the wear rate can be shifted by the evolution function f_w (compare transparent and solid lines). Table 6 lists the identified evolution parameters.

In a second validation step, the wear algorithm is applied to an LAT100 testing protocol (see Table 3). The corresponding FE model is shown in Fig. 14.

To run LAT simulations efficiently, an ALE approach is used. A two-dimensional axis-symmetric model represents a periodic sector of the revolved three-dimensional Grosch wheel, where the number of cross-section nodes coincides with the number of streamlines in the three-dimensional model. All

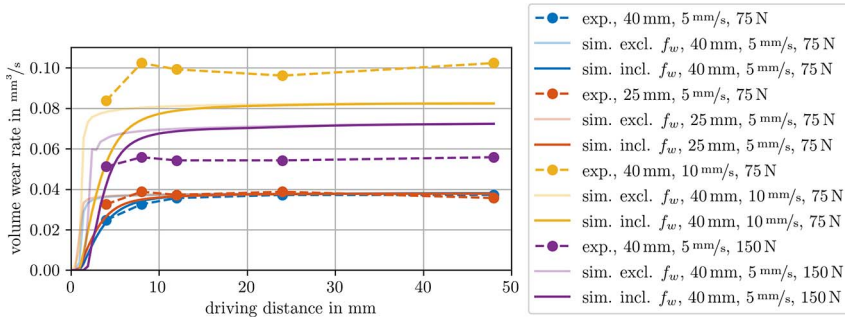

FIG. 13 — *Validation of wear rate using LFT at small driving distances.*

wheel nodes at the rim surface are fixed. Only a rotation around the y-axis is possible. The rim center is set to the global point of origin. Hence, the center point of the LAT disc in the reference configuration is calculated by

$$X_{\text{disc}} = \begin{bmatrix} 160\,\text{mm}\sin(\alpha) \\ -160\,\text{mm}\cos(\alpha) f_{\text{flip}} \\ -42\,\text{mm} \end{bmatrix}, \tag{32}$$

where f_{flip} is introduced as flip factor and α represents the slip angle measured at the center of the rigid rim. After each single LAT100 protocol test, the rubber wheel is rotated by 180° around the z-axis to ensure uniform wear at each wheel side, which is carried out by the flip factor that has either value $f_{\text{flip}} = 1$ (no flip) or $f_{\text{flip}} = -1$ (flip as 180° rotation). In analogy to the first validation example, the substrate surface (LAT disc) is pressed against the rubber wheel. The friction coefficient μ_{disc} follows the Huemer friction law (see "Friction Model"). During the ALE simulation, both the LAT disc and the rubber wheel are rotated by the rotational velocity Ω_{disc} and Ω_{wheel}, respectively. The rotational velocity of the disc is defined by

$$\Omega_{\text{disc}} = \frac{v_x}{160\,\text{mm}} f_{\text{flip}}, \tag{33}$$

whereas Ω_{wheel} is identified during simulation (in dependence of the slip angle α) so that the torque moment approaches 0. The Δd for each LAT100 protocol step is equal to the corresponding driving distances listed in Table 3 because the abrasion leads to minor changes in the model geometry. In Figs. 15 and 16, the distribution of the contact pressure and the sliding velocity, respectively, are shown at the contact patch of the rubber wheel for three selected conditions of the LAT100 protocol. The sections displayed in Figs. 15–17 have a length of approximately 15 mm and width of 19 mm (equal to rubber wheel width). Although the vertical load of the rubber wheel is always $F_z = 75$ N, the distribution of the pressure p_N differs due to the different slip angles as well as the application of the wear model.

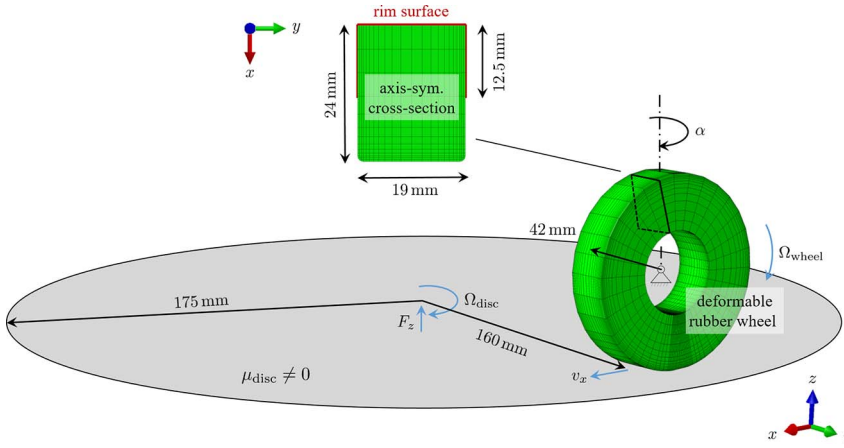

FIG. 14 — *FE model of LAT100.*

The sliding velocity $\| \boldsymbol{v}_T \|$ depends on the driving speed of the LAT disc and the Grosch wheel's slip angle. Figure 16 proves that the maximum values of $\| \boldsymbol{v}_T \|$ are close to the trailing edge of the contact zone. Furthermore, the slip angle affects the contact patch width: the larger α, the larger the width. Furthermore, Figs. 15 and 16 indicate that the extension of the friction map region is required (see $\mu_{\text{fit,out}}$ in Fig. 7), because LFT experiments are not performed at $p_N = 3.7\text{N/mm}^2$ and $\| \boldsymbol{v}_T \| = 2900\,\text{mm/s}$ with the applied rubber material.

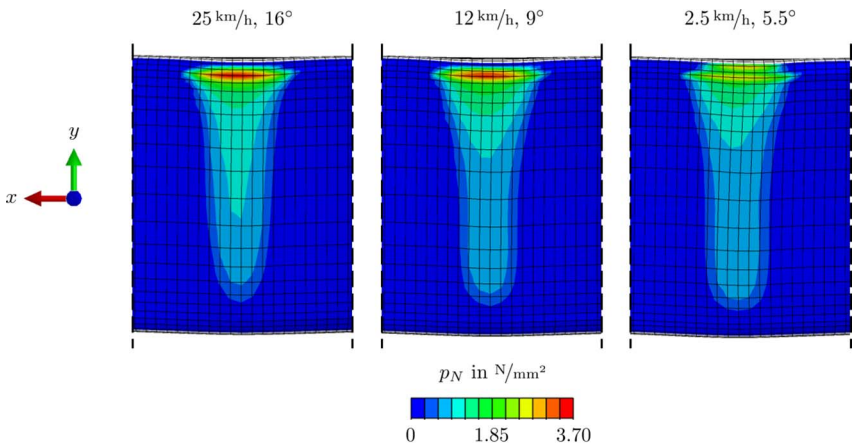

FIG. 15 — *Contact pressure distribution of LAT100 conditions selected from Table 3.*

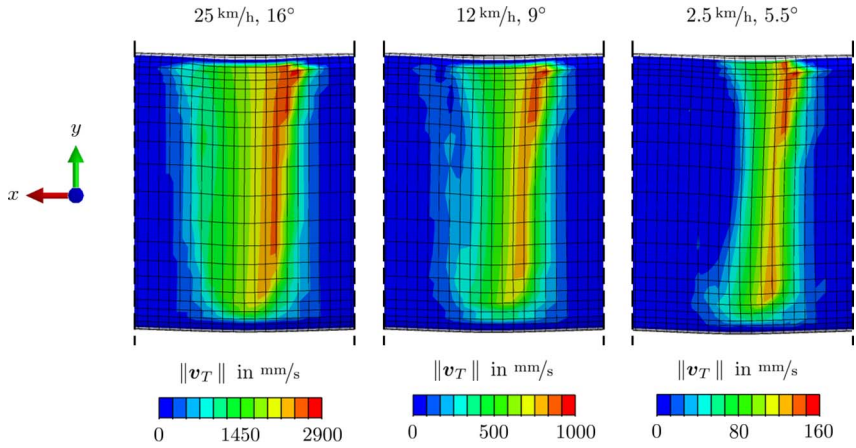

FIG. 16 — *Sliding velocity distribution of LAT100 conditions selected from Table 3.*

The implemented Huemer friction law results in the friction coefficient distribution μ shown in Fig. 17 on the left side for $v = 25\,\mathrm{km/h}$ and $\alpha = 16^{\circ}$. Note that the locations of the highest μ values do not match the locations of the contact pressure peaks from Fig. 15.

In the center of Fig. 17, the friction power intensity $\partial \dot{E}_f / \partial A$ is presented as consequence of the shear stress and the sliding velocity in the contact region. In combination with the evolution function f_w on the right side in Fig. 17, the friction power intensity leads to the wear energy rate intensity $\partial \dot{E}_w / \partial A$ and thus to the volume wear rate intensity $\partial \dot{V}_w / \partial A$. Note that the values of the evolution function f_w increase to the trailing edge of the rubber wheel as more frictional energy evolves into the rubber surface and then on the leading edge, where $f_w = 0$.

The resulting frictional energy rates of the entire rubber wheel are compared with experiments in Fig. 18. In [7], an approximation of the frictional energy rate of an LAT100 test is given by

$$\dot{E}_{f,\mathrm{LAT}} \approx F_y \, v_x \sin(\alpha)\,, \tag{34}$$

with F_y as side force measured at the rim of the rubber wheel. To prove the relationship in Eq. (34), the output of Eq. (34) is compared with the output of

$$\dot{E}_f = \sum_{i=1}^{n_{sl}} \sum_{j=1}^{n_{sec}} \| \boldsymbol{t}_{T,i,j} \| \, A_{i,j} \, \| \boldsymbol{v}_{T,i,j} \|, \tag{35}$$

which sums up the frictional energy rate from Eq. (12) over all sectors and streamlines in the simulation. Figure 18 validates the use of the approximation

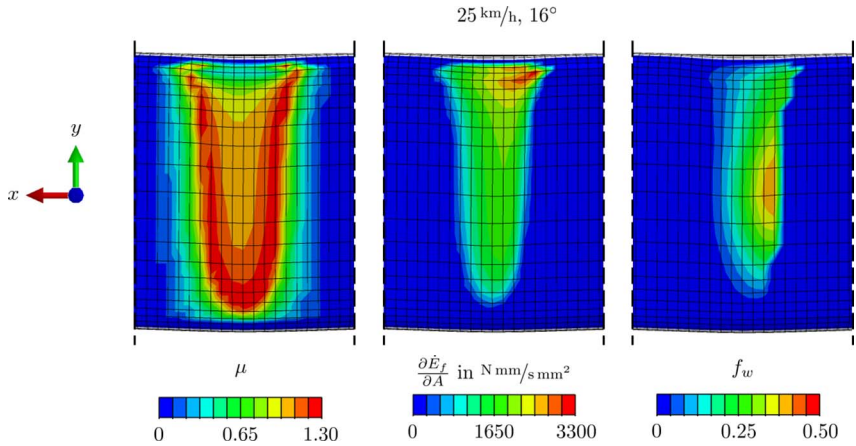

FIG. 17 — *Distribution of friction coefficient, frictional power intensity, and evolution function of LAT100 at* $v = 25\,km/h$ *and* $\alpha = 16^{\circ}$.

function (compare solid and dashed lines). In addition, Fig. 18 confirms that the LAT FE model and the material model as well as the underlying friction model are applicable.

Furthermore, the wear rate is analyzed for the LAT100 protocol listed in Table 3. Figure 19 compares the volume loss rate measured in experiments and resulted from simulation. The density of the rubber material is assumed to be $1.12 \times 10^{-3}\,g/mm^3$ [2]. The wear rate of tests using the same boundary conditions (speed and slip angle) are averaged. The red solid line is associated to the

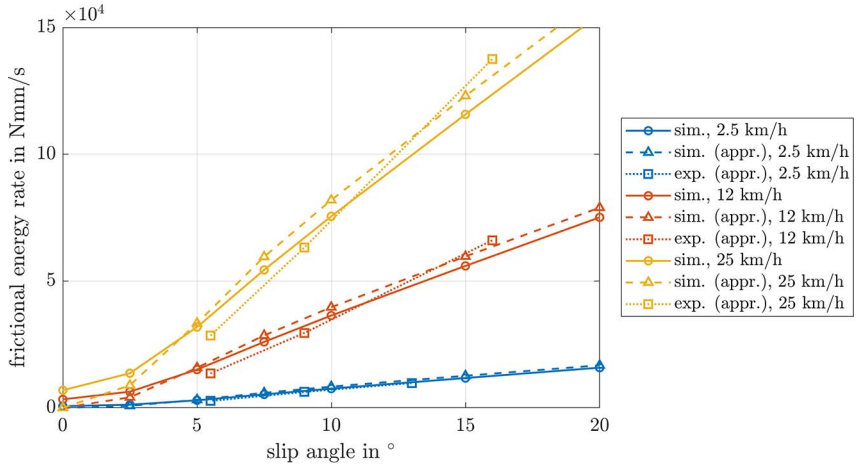

FIG. 18 — *Validation of frictional energy rate by using LAT.*

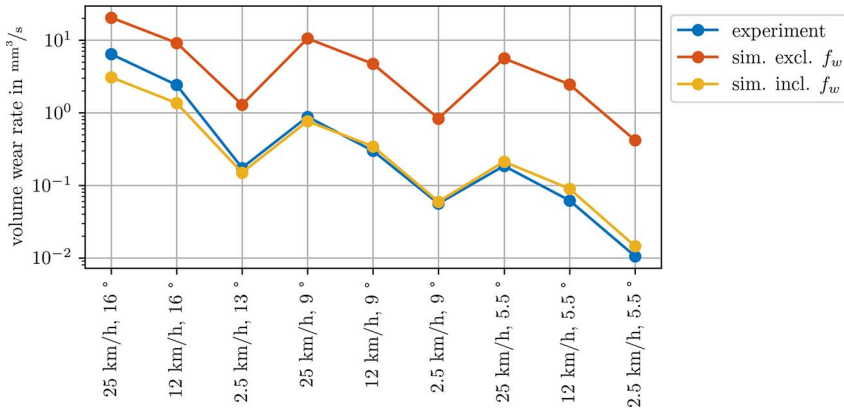

FIG. 19 — *Validation of wear rate by using LAT.*

simulation output without the application of the energy evolution law introduced in Eq. (16). Hence, the wear rate is overestimated significantly, which is also shown in Fig. 8, where the output of LFT tests is up to factor of 25 higher than the LAT results. However, the inclusion of the evolution law let the simulation output fits well to the LAT100 wear experiments. Figure 19 proves the necessity of the wear energy approach for predicting rolling frictional abrasion. Note that the applied evolution parameters are identical to the parameters used for the short-distance sliding Grosch wheel segments (parameters are listed in Table 6).

The change of the contact nodes during simulation of the LAT100 protocol is visualized in Fig. 20. For reason of visibility, only the unworn and three different conditions are plotted. Furthermore, Fig. 20 shows the influence of the flip factor (f_{flip}). For each protocol condition, the right edge is abraded first, followed by the left edge.

The re-mesh algorithm introduced in "Wear Model" minimizes the differences between computed wear volume using Eq. (13) and re-meshed wear volume until the criterion in Eq. (29) is fulfilled or a maximum of iterations is reached. The final deviation of computed and re-meshed wear volume is shown in Fig. 21 excluding and including the Newton–Raphson iteration as re-mesh algorithm.

The deviation of computed and re-meshed wear volume is calculated by

$$\epsilon_w = \frac{V_{w,r}}{V_{w,c}} - 1, \tag{36}$$

where $V_{w,c}$ and $V_{w,r}$ is the total computed wear volume and the total wear volume after re-meshing, respectively. If the Newton–Raphson iteration during re-

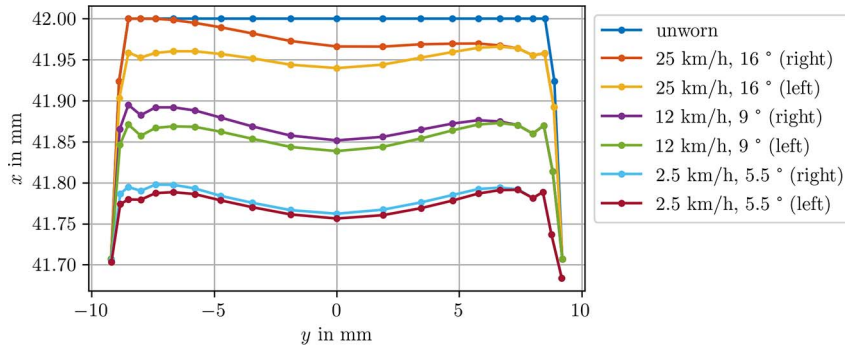

FIG. 20 — *Resulting worn node coordinates of the axis-symmetric cross section by using the LAT protocol including the wear energy evolution approach.*

meshing is not used (legend entry "excl. NR"), the wear displacement factor $w_I = V_{w,I}/A$ at node I is equal to the computed wear volume divided by the corresponding nodal contact area. Except for the last three conditions, where the abrasion affects the left side of the wheel, the deviation between computed and re-meshed wear volume can be decreased by the proposed re-mesh algorithm. However, for every LAT100 protocol condition, the range of the discrepancy to the computed nodal wear volume is reduced, as is illustrated in Fig. 22.

In each boxplot in Fig. 22, the difference between computed and re-meshed wear volume of all nodes in the final time step of the corresponding protocol test is shown. The bottom bar and the top bar in Fig. 22 refer to $Q_1 - 1.5\,IQR$

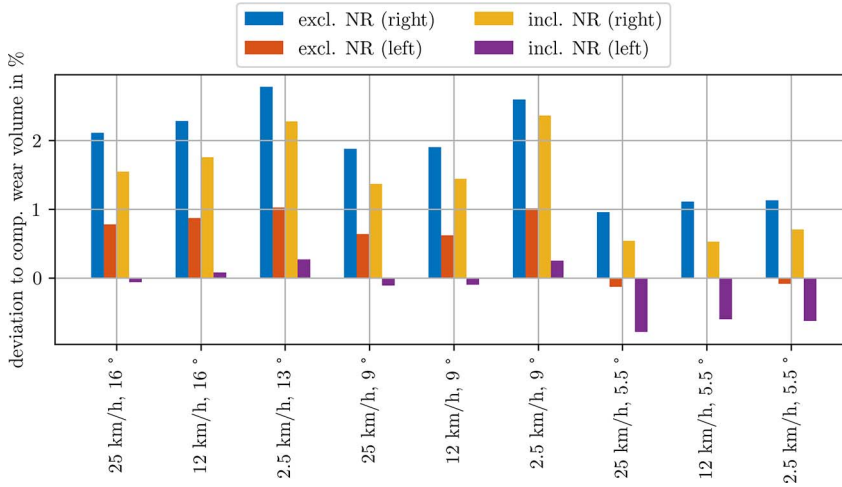

FIG. 21 — *Computed vs re-meshed (total) wear volume.*

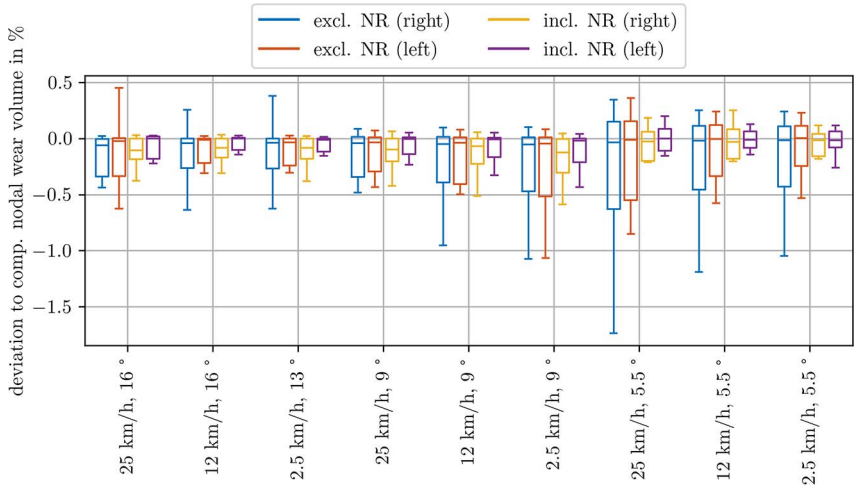

FIG. 22 — *Computed vs re-meshed (nodal) wear volume.*

and $Q_3 + 1.5\,IQR$, respectively, with $IQR = Q_3 - Q_1$ as interquartile range. The quartiles $Q_1 = q(25\%)$ and $Q_3 = q(75\%)$ are denoted as first and third quartiles (lower and upper box bar), respectively, and $Q_2 = q(50\%)$ coincides with the median (bar within box). In Fig. 23, the number of re-mesh runs per LAT100 protocol conditions and the averaged number of re-mesh iterations per re-mesh run are shown.

The number of re-mesh runs depends on the number of sectors of the LAT model that are in contact during ALE simulations (see Fig. 14). For each time step, in which nodes interact with the substrate, the re-mesh procedure is conducted. In most cases, the re-mesh algorithm requires only one iteration to minimize the deviation between computed and re-meshed wear volume, i.e., Eq. (29) is satisfied. In contrast to the computation time of the FEM simulations, the time needed to perform the postprocessing procedure including the Newton–Raphson iterations is neglectable (1–2% of the simulation time). To summarize the validation on LAT100, the application of the re-mesh algorithm including the Newton–Raphson iteration reduces the deviation of the total computed wear volume vs volume loss as consequence of mesh modification by approximately 43% (calculated from Fig. 21). On node level, the gap to computed nodal wear volume is decreased by 93% on average compared with remeshing without the Newton–Raphson iteration (obtained from Fig. 22).

Conclusions and Outlook

In this work, a wear model based on friction power intensity in combination with a sophisticated re-mesh algorithm is developed as a holistic simulation

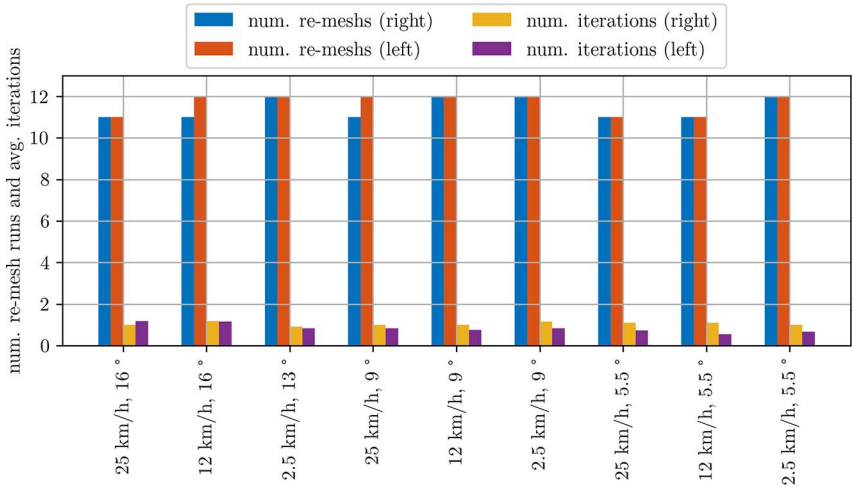

FIG. 23 — *Number of re-mesh runs per test condition and averaged number of re-mesh iterations per re-mesh run.*

framework. Furthermore, a wear energy rate evolution law is introduced to predict frictional abrasion on rolling rubber wheels, where the transition from deformation slip to sliding slip is taken into account. LFT friction tests and LFT abrasion tests on block level at different loads and sliding velocities are conducted to identify the friction features and wear model parameters because a correlation between frictional energy rate and wear rate is documented. It is possible to reduce the deviation between computed wear volume and volume loss caused by mesh modification using the implemented re-mesh algorithm (algorithm validation). In addition, the simulation framework is validated by LFT tests at small sliding distances (sliding abrasion) as well as LAT protocol (rolling abrasion).

The friction model parameters are obtained by LFT tests by using sandpaper grit 60, because the friction features are comparable to an LAT disc grit 60 (see Fig. 4). However, it is recommended to apply the same substrate in future research. The identified parameters of the wear model parameters as well as the wear energy evolution are linked to the applied contact partners, rubber and LAT disc grit 60. To reduce the number of laboratory friction and abrasion tests as soon as the composition of rubber or substrate changes, a correlation between the surface textures and the material properties toward the resistance of abrasion has to be secured.

Furthermore, the friction formulation can be extended to depend on the contact temperature, although temperature is not only an input variable but also an output variable, because the rubber blocks heat up due to friction. The introduced wear model may consider thermal effects because it relies on frictional

energy (rate). The proposed wear simulation framework is a postprocessing analysis, i.e., no mesh update during the FEM simulation is performed. Hence, the frequency of re-mesh updates has to be investigated depending on the driving conditions to obtain the impact on contact quantities (e.g., pressure, sliding velocity). It is required to understand the physical reason and effect of rolling frictional abrasion to the full extent to prove the applicability of the wear energy rate evolution approach. Because the simulation framework including the re-mesh algorithm is able to process non–axis-symmetric models, the proposed energy evolution approach can be investigated on full tire level. In addition, the analysis of multiple (parallel) driving conditions (e.g., free-rolling, braking, acceleration, cornering, combined braking-cornering) can be carried out as described in [20].

Acknowledgments

This research work is funded by the Deutsche Forschungsgemeinschaft (German Research Foundation)–SFB/TRR 339, Project-ID 453596084, Subproject INF. This project received funding by the European Union's Horizon 2020 research and innovation program under grant agreement number 958174. This project is co-financed by tax revenues on the basis of the budget adopted by the Saxon State Parliament. The support of CEAT Tyres Ltd., Leibniz Universität Hannover, and Technische Universität Dresden is gratefully acknowledged.

References

[1] Moldenhauer, P. and Kröger, M., "Simulation and Experimental Investigations of the Dynamic Interaction between Tyre Tread Block and Road," in Besdo, D., Heimann, B., Klüppel, M., Kröger, M., Wriggers, P., and Nackenhorst, U. (eds.), *Elastomere Friction: Theory, Experiment and Simulation*, Springer, Berlin, 2010, pp. 165–200, https://doi.org/10.1007/978-3-642-10657-6_6

[2] Hartung, F., Garcia, M. A., Berger, T., Hindemith, M., Wangenheim, M., and Kaliske, M., "Experimental and Numerical Investigation of Tire Tread Wear on Block Level," *Lubricants*, Vol. 9, 2021, p. 113, https://doi.org/10.3390/lubricants9120113

[3] Kahms, S. and Wangenheim, M., "Experimental Investigation and Simulation of Aircraft Tire Wear," *Tire Science and Technology*, Vol. 49, 2021, pp. 55–74, https://doi.org/10.2346/tire.20.180201

[4] Grosch, K. A., "Rubber Abrasion and Tire Wear," *Rubber Chemistry and Technology*, Vol. 81, 2008, pp. 470–505, https://doi.org/10.5254/1.3548216

[5] Nguyen, V., Zheng, D., Schmerwitz, F., and Wriggers, P., "An Advanced Abrasion Model for Tire Wear," *Wear*, Vol. 396, 2018, pp. 75–85, https://doi.org/10.1016/j.wear.2017.11.009

[6] Li, Z., Li, Z., and Wang, Y., "An Integrated Approach for Friction and Wear Simulation of Tire Tread Rubber. Part I: Friction Test, Characterization and Modeling," *Tire Science and Technology*, Vol. 48, 2020, pp. 123–145, https://doi.org/10.2346/tire.19.170174

[7] Li, Z., Li, Z., and Wang, Y., "An Integrated Approach for Friction and Wear Simulation of Tire Tread Rubber. Part II: Wear Test, Characterization and Modeling," *Tire Science and Technology*, Vol. 48, 2020, pp. 146–165, https://doi.org/10.2346/tire.19.170175

[8] Salehi M. , "Prediction of Tire Grip: A New Method for Measurement of Rubber Friction under Laboratory Conditions," Ph.D. Dissertation, University of Twente, Enschede, The Netherlands, 2020.
[9] Archard, J. F., "Contact and Rubbing of Flat Surfaces," *Journal of Applied Physics*, Vol. 24, 1953, pp. 981–988, https://doi.org/10.1063/1.1721448
[10] Schallamach, A. and Turner, D., "The Wear of Slipping Wheels," *Wear*, Vol. 3, 1960, pp. 1–25, https://doi.org/10.1016/0043-1648(60)90172-1
[11] Braghin, F., Cheli, F., Melzi, S., and Resta, F., "Tyre Wear Model: Validation and Sensitivity Analysis," *Meccanica*, Vol. 41, 2006, pp. 143–156, https://doi.org/10.1007/s11012-005-1058-9
[12] Tamada, R. and Shiraishi, M., "Prediction of Uneven Tire Wear Using Wear Progress Simulation," *Tire Science and Technology*, Vol. 45, 2017, pp. 87–100, https://doi.org/10.2346/tire.17.450201
[13] Kahms, S., Hindemith, M., and Wangenheim, M., "Thermomechanical Modeling of Aircraft Tire–Runway Contact for Transient Maneuvers," *Tire Science and Technology*, Vol. 51, 2023, 22012, https://doi.org/10.2346/tire.23.22012
[14] Kern. Available at: https://www.kern-sohn.com/shop/en/products/laboratory-balances/precision-balances/ Accessed March 2024.
[15] Wriggers, P., *Computational Contact Mechanics*, Springer, Berlin, 2006, https://doi.org/10.1007/978-3-540-32609-0
[16] Huemer, T., Liu, W., Eberhardsteiner, J., and Mang, H., "A 3D Finite Element Formulation Describing the Frictional Behavior of Rubber on Ice and Concrete Surfaces," *Engineering Computations*, Vol. 18, 2001, pp. 417–437, https://doi.org/10.1108/02644400110387109
[17] Kaliske, M., Serafinska, A., and Zopf, C., "Optimized and Robust Design of Tires Based on Numerical Simulation," *Tire Science and Technology*, Vol. 41, 2013, pp. 21–39, https://doi.org/10.2346/tire.13.410103
[18] Behnke, R. and Kaliske, M., "Thermo-mechanically Coupled Investigation of Steady State Rolling Tires by Numerical Simulation and Experiment, *International Journal of Non-Linear Mechanics*, Vol. 68, 2015, pp. 101–131, https://doi.org/10.1016/j.ijnonlinmec.2014.06.014
[19] Nackenhorst, U., "The ALE-Formulation of Bodies in Rolling Contact: Theoretical Foundations and Finite Element Approach," *Computer Methods in Applied Mechanics and Engineering*, Vol. 193, 2004, pp. 4299–4322, https://doi.org/10.1016/j.cma.2004.01.033
[20] Zheng, D., "Prediction of Tire Tread Wear with FEM Steady State Rolling Contact Simulation," *Tire Science and Technology*, Vol. 31, 2003, pp. 189–202, https://doi.org/10.2346/1.2135268